CHEMISTRY OF MATERIALS

Composition-Dependent Electrocatalytic Activity of Zn-Doped Ni_5P_4 Nanocrystals for the Hydrogen Evolution Reaction

Lisa S. Graves, Rajib Sarkar, Ka Un Lao, and Indika U. Arachchige*

Cite This: *Chem. Mater.* 2023, 35, 6966−6978

Read Online

ACCESS | Metrics & More | Article Recommendations | Supporting Information

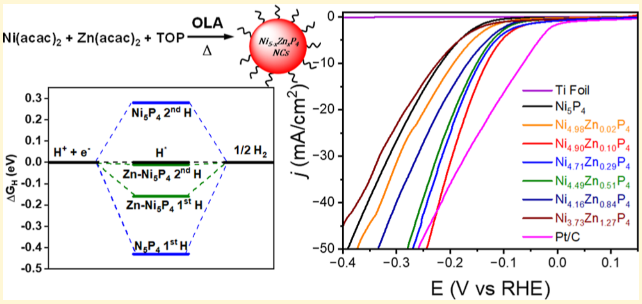

ABSTRACT: Electrocatalytic water splitting presents an exciting opportunity to produce environmentally benign hydrogen fuel to power human activities. Earth-abundant Ni_5P_4 has emerged as an efficient catalyst for the hydrogen evolution reaction (HER), and its activity can be enhanced by admixing synergistic metals to modify the surface affinity and consequently the kinetics of HER. Computational studies suggest that the HER activity of Ni_5P_4 can be improved by Zn doping, causing a chemical pressure-like effect on Ni_3 hollow sites. Herein, we report a facile colloidal route to produce $Ni_{5-x}Zn_xP_4$ nanocrystals (NCs) with control over structure, morphology, and composition and investigate their composition-dependent HER activity in alkaline solutions. $Ni_{5-x}Zn_xP_4$ NCs retain the hexagonal structure and solid spherical morphology of binary Ni_5P_4 NCs, with a notable size increase from 9.2−28.5 nm for $x = 0.00−1.27$ compositions. Elemental maps affirm the homogeneous ternary alloy formation with no evidence of Zn segregation. Surface analysis of $Ni_{5-x}Zn_xP_4$ NCs indicates significant modulation of the surface polarization upon Zn incorporation, resulting in a decrease in $Ni^{\delta+}$ and an increase in $P^{\delta-}$ charges. Although all compositions followed a Volmer−Heyrovsky HER mechanism, the modulated surface polarization enhances the reaction kinetics, producing lower Tafel slopes for $Ni_{5-x}Zn_xP_4$ NCs (82.5−101.9 mV/dec for $x = 0.10−0.84$) compared to binary Ni_5P_4 NCs (109.9 mV/dec). $Ni_{5-x}Zn_xP_4$ NCs showed higher HER activity with overpotentials of 131.6−193.8 mV for $x = 0.02−0.84$ in comparison to Ni_5P_4 NCs (218.1 mV) at a current density of −10 mA/cm². Alloying with Zn increases the material's stability with only a ∼10% increase in overpotential for $Ni_{4.49}Zn_{0.51}P_4$ NCs at −50 mA/cm², whereas a ∼33% increase was observed for Ni_5P_4 NCs. At current densities above −40 mA/cm², bimetallic NCs with $x = 0.10$, 0.29, and 0.51 compositions outperformed the benchmark Pt/C catalyst, suggesting that hexagonal alloyed $Ni_{5-x}Zn_xP_4$ NCs are excellent candidates for practical applications that necessitate lower HER overpotentials at higher current densities.

■ INTRODUCTION

The effects of climate change as a result of global warming continue to drive the development of clean and sustainable energy sources. One such promising carbon neutral source is hydrogen (H_2) fuel, which can be generated conveniently through the phenomenon of water splitting.[1] To date, the best performing electrocatalytic devices for water splitting reactions are composed of expensive and rare materials such as platinum, iridium, and ruthenium,[2−4] which are not favorable for widespread usage. Transition metal phosphides, specifically nickel phosphides, are abundant and cost-effective materials that have previously been found to be exceptional catalysts for various hydrotreating reactions,[5,6] such as hydrodenitrogenation,[7] hydrodesulfurization,[8] hydrodeoxygenation,[9] and relatively recently have also been found to be promising candidates for the hydrogen evolution reaction (HER).[10,11]

Out of the seven stable nickel phosphides, hexagonal Ni_5P_4 has been shown to be the most efficient bulk material for HER, as evident by its low overpotential, fast kinetics, and stability in both acidic and alkaline solutions.[10,12−15] Laursen and coauthors examined the HER efficiency of micron-sized aggregates of Ni_5P_4 particles and compared their performance to benchmark electrocatalytic materials.[15] Under acidic conditions, Ni_5P_4 particles displayed an overpotential (η) of 23 mV and slightly outperformed the polished Pt foil (27 mV), whereas under alkaline conditions, the same material overperformed what was considered the most efficient noble-metal-free standard at that time, amorphous Ni−Mo alloys, with overpotentials of 49 and 82 mV, respectively, at a current density (j) of −10 mA/cm². Within the nano-regime, a decrease in activity was reported when Pan and co-workers investigated the HER efficiency of tetragonal $Ni_{12}P_5$ (hollow nanoparticles (NPs) of 17.55 nm), hexagonal Ni_2P (hollow NPs of 9.19 nm), and hexagonal Ni_5P_4 (solid NP aggregates of

Received: May 19, 2023
Revised: August 1, 2023
Published: August 14, 2023

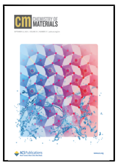

https://doi.org/10.1021/acs.chemmater.3c01229

600 nm) in acids and observed η_{-10} of 208, 137, and 118 mV, respectively.[12] Tafel analysis revealed a lower slope and faster HER kinetics for Ni_5P_4 NPs (42 mV dec^{-1}) compared to $Ni_{12}P_5$ (75 mV dec^{-1}) and Ni_2P (49 mV dec^{-1}) NPs, and a Volmer−Heyrovsky HER mechanism was proposed for all three phases. Li et al. examined the HER activity of ∼5.6 nm Ni_5P_4 NCs, where a higher HER activity was reported (η_{-10} = 103 mV), which has been attributed to the high surface area of smaller, discrete NCs.[16]

As an efficient HER catalyst, the Ni_5P_4 (001) plane[12,14,17] is known as the most active and stable catalytic surface.[18] However, the catalytic activity of the Ni_5P_4 (001) surface is not optimal for water splitting because the Ni_3 hollow[19,20] and P-top sites[21] bind too strongly to hydrogen, impeding the facile removal of H_2. Although it has been suggested that the number of Ni_3 hollow sites can be decreased by increasing the abundance of P on the (001) surface,[22] the added P-top sites[23] on the P-terminated Ni_5P_4 bond too weakly to hydrogen, causing a substantial decrease in the HER activity. Furthermore, it has been reported that Ni_5P_4 (001) does not favor additional P on the surface under normal synthetic conditions[17] and is different from Ni_2P (001) reflection, which favors P enrichment according to both experimental and computational studies.[17,24] Thus, to further improve the HER activity, an increase in surface metal sites along with a systematic modulation of the surface affinity is needed, which can be achieved via heteroatom doping. Moreover, heteroatom doping is expected to stabilize hexagonal Ni_5P_4 and therefore increase both the HER activity and corrosion tolerance.[17,25] To date, a few studies on transition metal-doped Ni_5P_4 materials have been reported. These studies demonstrated enhanced HER activity of porous Ni_5P_4 microstructures doped with Fe,[26,27] Co,[27,28] V,[23] Se,[29] Cu,[27] and Ru[21] in acids and alkali. Under alkaline conditions, Ru doping improved the HER activity by decreasing the η_{-10} to 123 mV compared to 289 mV for Ni_5P_4. Under an acidic environment, Co (6.6% at.) doping[28] decreased the η_{-10} to 310 mV from 410 mV of binary Ni_5P_4. Admixing of V resulted in improved HER activity under acidic and pH-neutral conditions. Interestingly, the concentration of the dopant also influences the HER activity, where 20% Co−Ni_5P_4 showed a significant decrease in η_{-10} to 100.5 mV, while 10%, 30% Co, and pristine Ni_5P_4 showed η_{-10} of 159.5, 139.5, and 193.2 mV, respectively. Computational studies suggest that the concentration of the heteroatom modulates the surface affinity, which ultimately impacts the binding interactions between the catalyst and adsorbed H species.[27] Although these reports demonstrate improved HER activity for heteroatom-doped Ni_5P_4 nanosheets and microstructures, the synthesis and HER activity of discrete, heteroatom-doped Ni_5P_4 NCs have not been thoroughly investigated.

Herein, density functional theory (DFT) was utilized to explore the influences of various transition metal dopants on the binding energy of hexagonal Ni_5P_4, where Zn proved to be the most promising dopant that lowered the first and second hydrogen adsorption free energy (ΔG_H) from −0.43 to −0.16 and 0.28 to −0.01 eV, respectively. Accordingly, phase pure $Ni_{5-x}Zn_xP_4$ NCs were synthesized colloidally, and HER activity was investigated as a function of composition. $Ni_{5-x}Zn_xP_4$ NCs retained the solid nanocrystal morphology and hexagonal structure of Ni_5P_4 with an increase in particle size from 9.2 to 28.5 nm for x = 0.0−1.27 (0.0−16.67%) compositions. $Ni_{5-x}Zn_xP_4$ NCs with compositions up to x = 0.02−0.84 showed lower η_{-10} from 131.6 to 193.8 mV, compared to 218.1 mV of Ni_5P_4, with the lowest η_{-10} achieved at x = 0.10. At higher j values (>−40 mA/cm^2), $Ni_{4.90}Zn_{0.10}P_4$, $Ni_{4.71}Zn_{0.29}P_4$, and $Ni_{4.49}Zn_{0.51}P_4$ NCs outperformed the benchmark Pt/C. In addition, Tafel slopes were observed to decrease from 109.9 mV/dec for Ni_5P_4 to 82.5−101.9 mV/dec for the $Ni_{5-x}Zn_xP_4$ NCs (x = 0.10−0.84). To the best of our knowledge, this is the first work that encompasses a theoretical approach to systemically investigating the atomic-scale implications of heteroatom doping while experimentally comparing the HER activity of discrete Zn-doped Ni_5P_4 NCs. The insight incurred through this study will be an additional tool in understanding how material performance can be manipulated through electronic structure modulations in the synthetic development of high-efficiency (electro)catalysts.

■ EXPERIMENTAL SECTION

Materials. Nickel (II) 2,4-pentanedionate ($Ni(acac)_2$, 95%) and bis(2,4-pentanedionato) zinc (II) ($Zn(acac)_2$, 96.0%) were purchased from Fischer. Tri-*n*-octylphosphine (TOP, 97%) was purchased from Strem Chemical. Oleylamine (OLA technical grade, 70%), toluene, and ethanol were purchased from Fisher. Carbon-coated 200 mesh copper grids were purchased from SPI Supplies. Titanium foil (thickness 0.25 mm; 99.7%) and platinum on graphitized carbon (Pt/C, 10% wt) were purchased from Sigma-Aldrich. Graphite rods (6.15 mm × 102 mm, 99.99995%) were purchased from Alfa Aesar. A Hg/HgO reference electrode filled with 1 M NaOH solution was purchased from CH Instruments. Pelco colloidal silver paint was purchased from Ted Pella. Henkel Loctite EA-E00NS epoxy adhesive was purchased from Ellsworth Adhesives. Chemical-resistant PTFE-insulated silver-plated copper wire was purchased from McMaster-Carr. OLA was dried under vacuum for 3 h prior to use. Toluene was dried over Na metal, and ethanol was dried over CaO and molecular sieves and then distilled under N_2 prior to use.

Synthesis of Ni_5P_4 NCs. The synthesis of Ni_5P_4 NCs was adapted from the literature.[30] In a glovebox, 0.67 mmol of Ni $(acac)_2$ was combined with 10.0 mL of OLA and 5.0 mL of TOP in a 50 mL round bottom flask and attached to a Schlenk line. The solution was degassed under vacuum at 120 °C for at least 20 min. After degassing, a steady flow of nitrogen gas was introduced, and the flask was wrapped in glass wool before the temperature was increased to 340 °C. Once at 340 °C, the solution was kept under reflux for 4 h. After 4 h, the reaction was cooled to room temperature, and NCs were isolated with a mixture of toluene and excess ethanol and then centrifuged at 6000 rpm for 10 min. This purification process was repeated a minimum of 3 times, and the final NC product was dried under vacuum.

Synthesis of $Ni_{5-x}Zn_xP_4$ NCs. The synthesis of $Ni_{5-x}Zn_xP_4$ NCs was modified from the synthesis of Ni_5P_4 NCs. In a typical synthesis, $Ni(acac)_2$ and $Zn(acac)_2$ were combined with 10.0 mL of OLA and 5.0 mL of TOP in a 50 mL round bottom flask and attached to a Schlenk line. The solution was degassed at 120 °C for a minimum of 20 min, after which the solution was purged with nitrogen gas, and the flask was wrapped in glass wool before the temperature was increased to 340 °C. The solution was kept under reflux at 340 °C for 4 h, and the purification procedure remained unchanged.

Physical Characterization. Powder X-ray diffraction (PXRD) patterns were recorded using an Empyrean Multipurpose X-ray Diffractometer equipped with a Cu Kα (λ = 1.5418 Å) radiation source under 45 kV and 40 mA operating conditions. The Scherrer formula was used to manually calculate the crystallite size based on the hexagonal Ni_5P_4 (214) reflection.[31] Low resolution transmission electron microscopy (TEM) images were acquired using a Jeol JEM-1400Plus transmission electron microscope equipped with a Gatan UltraScan 4000SP 4k × 4k CCD camera, operating at 120 kV. High-resolution TEM, scanning transmission electron microscopy (STEM) images, and elemental maps were attained using a JEM-F200 Cold FEG Electron Microscope operating at an accelerating voltage of 200

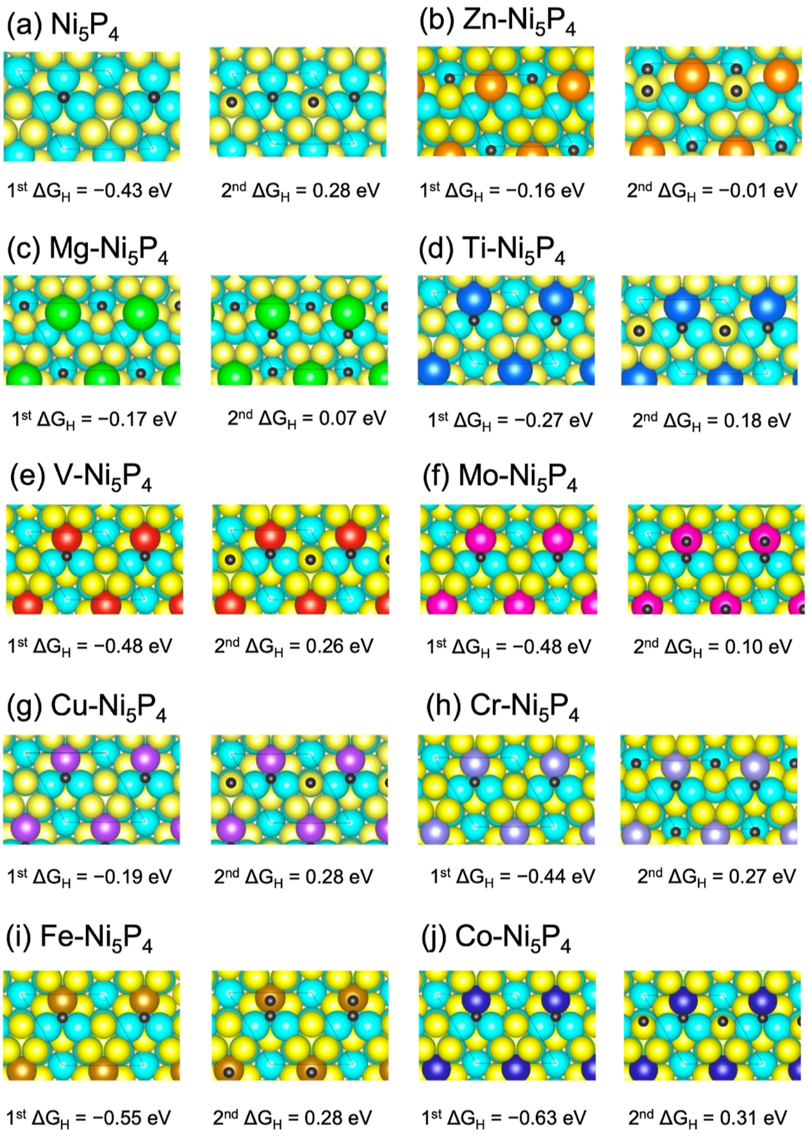

Figure 1. Lowest 1st and 2nd ΔG_H in eV on pristine Ni_5P_4 (001) (a) with the Ni_3P_3 termination, and the corresponding nine transition-metal-doped (b) Zn, (c) Mg, (d) Ti, (e) V, (f) Mo, (g) Cu, (h) Cr, (i) Fe, and (j) Co surfaces calculated by PBE+D3(BJ).

kV and equipped with an energy dispersive X-ray analyzer. Sample preparation for TEM/high resolution (HR)TEM involved drop casting a 10 μL aliquot of a dilute $Ni_{5-x}Zn_xP_4$ NC-toluene solution onto carbon-coated 200 mesh copper grids, and residual toluene was allowed to evaporate prior to imaging. Elemental compositions were determined through inductively coupled plasma-optical emission spectroscopy (ICP-OES) using an Agilent Technologies 5110 ICP-OES equipped with an Agilent Technologies SPS4 autosampler. Samples were digested in acid (3:1 v/v HCl/HNO_3) and placed in a warm water bath (~60 °C) for 24 h to ensure complete digestion, and then further diluted 15 times with Milli-Q-filtered water prior to analysis. X-ray photoelectron spectra (XPS) were recorded using a PHI VersaProbe III Scanning XPS Microprobe. NC samples were annealed in a 5% H_2:Ar environment at 300 °C for 4 h prior to XPS analysis. Regional scans were completed using a pass energy of 26.00 eV with 20 ms per step, and the number of sweeps was dependent upon the signal intensity of each element. Energy dispersive spectra were recorded using a Hitachi Ultra High-Resolution Analytical FE-SEM SU-70, operating at 15 kV and equipped with an energy dispersive X-ray analyzer (SEM-EDS). Ni, Zn, and P concentrations were determined by taking the average composition for each element at 5 separate locations along the sample. FT-IR spectra were recorded using a Thermo Scientific Nicolet iS50 FTIR.

Computational Studies. To investigate the most active metal-doped Ni−P material, the HER activity of the Ni_5P_4 (001) surface doped with a range of synergistic metals (Zn, Mg, Ti, V, Mo, Cu, Cr, Fe, and Co) was investigated using density functional theory (DFT) within the Vienna Ab initio Simulation Package (VASP)[32] and the projector-augmented-wave (PAW) method. The electrocatalytic performance was examined by computing the Gibbs free energy (ΔG) for HER,[33,34] $\Delta G_H = \Delta E + \Delta E_{ZPE} - T\Delta S$, where ΔE, ΔE_{ZPE}, T, and ΔS represent the electronic adsorption energy calculated by DFT, zero-point energy, temperature, and entropy contributions, respectively. *A* factor of 0.24[35,36] or 0.25 eV[20,37] was used to account for all the contributions in entropic and zero-point energy ($\Delta E_{ZPE} - T\Delta S$). We use 0.24 eV to account for such a contribution here, and then ΔG_H is simplified into ΔE + 0.24 eV. Based on the Bell−Evans−Polanyi principle, the computationally demanding calculations of reaction barriers can be avoided, and we can only focus on ΔG binding interactions in this study.[38] Since HER involves hydrogen adsorption on the catalyst site, the ΔG_H binding interaction is regarded as the most important descriptor for intrinsic HER activity.[39] The ideal catalyst can be probed with a ΔG_H value near 0 eV, in line with the Sabatier principle that the hydrogen should neither bind too weakly nor too strongly to the surface.[40,41] Because of the influence of $\Delta G_H \approx 0$ from the computational level,[42−44] $|\Delta G_H| < 0.1$ eV was chosen as an optimal criterion[40] to probe the highest active metal-doped Ni_5P_4 NCs. The Perdew−Burke−Ernzerhof (PBE) functional[45] was used to obtain structures, and PBE with the Grimme D3(BJ) dispersion correction[46,47] was used to calculate ΔE. A periodically repeated slab with six layers and a 15 Å vacuum, where the atoms at the bottom layer were fixed to their bulk positions, was used to model ΔG_H on the Ni_5P_4 (001) surface with the highest stable Ni_3P_3 termination.[22] A plane wave cut-off energy of 520 eV and a Γ-centered 5 × 5 × 1 grid of *k*-points were employed.

Fabrication of Working Electrodes. Working electrodes for HER were fabricated with $Ni_{5-x}Zn_xP_4$ NCs and commercial Pt/C catalyst on Ti foil substrates. Ti foils were cut into pieces of 0.5 cm × 0.4 cm area and subjected to sonication in a solution of acetone and ethanol (1:1, v/v) for 10 min. These foils were then treated with a mixture of 1 M HCl and 30% H_2O_2 (1:1, v/v) for 20 min, followed by an additional sonication in Milli-Q water (18 Ω). The catalyst ink solution was prepared by mixing 4 mg of $Ni_{5\text{-}x}Zn_xP_4$ or commercial Pt/C, 380 μL isopropanol, and 20 μL of Nafion, followed by sonication for 10 min in an ice water bath. Nafion was used to facilitate the adhesion of the catalysts onto the Ti substrate. A total of 40 μL of the catalyst was loaded to the Ti foil in 10 μL increment drops. Each aliquot of ink was dried in air before each successive addition. To improve the adhesion of the catalyst NCs onto theTi support and to remove organic ligands, the catalyst coated Ti foils were annealed inside a tube furnace at 300 °C for 4 h under 5% H_2/Ar gas flow. Ag paint was used to attach and establish proper ohmic contact between the NC-coated Ti foil and the Ag-plated Cu wire. Finally, a two-part epoxy was used to cover and insulate the Ag paint and Cu wire while leaving the catalytic area (0.20 cm^2) exposed for HER studies. The epoxy was left to dry for 24 h prior to electrocatalytic experiments.

Electrochemical Measurements. The electrochemical HER performance of $Ni_{5-x}Zn_xP_4$ NCs and commercial Pt/C was investigated using a CHI 760E electrochemical workstation. All experiments were carried out in a nitrogen-saturated 1 M KOH solution at room temperature and atmospheric pressure within a conventional three-electrode electrochemical cell. A carbon rod was used as the counter electrode, Hg/HgO (1 M NaOH) was used as the reference electrode, and catalyst-coated Ti foil served as the working electrode. Prior to data collection, N_2 gas was purged into the electrolyte solution for 1 h to remove atmospheric gas and maintain a N_2 blanket throughout the experiment. The potentials were reported with respect to the scale of reversible hydrogen electrode (RHE) potential by using the conversion formula: $E_{RHE} = E_{Exp} + E^0_{Hg/HgO} + 0.05916$ pH. The current density (j, mA/cm^2) of the catalyst was calculated by dividing the experimental current with the geometrical area of the electrode surface (0.2 cm^2). Cyclic voltammetry (CV) was conducted by sweeping the potential from 0.2 to 0.1 V at different scan rates to electrochemically clean and activate the catalyst. Linear sweep voltammetry (LSV) was utilized to record the polarization curve by scanning the potential from 0.2004 to −0.4996 V (vs RHE) at a scan rate of 5 mV/s. To examine the potential change over10 h of continuous HER, the stability of the catalyst was evaluated using chronopotentiometry (CP) operating at a constant j = −10 and −20 mA/cm^2.

■ RESULTS AND DISCUSSION

Theoretical Calculations of Heteroatom-Doped Ni_5P_4.

The lowest first and second ΔG_H on pristine and transition-metal-doped (Zn, Mg, Ti, V, Mo, Cu, Cr, Fe, and Co) Ni_5P_4 (001) surfaces with the Ni_3P_3 termination and their corresponding configurations are shown in Figure 1. The first hydrogen on the pristine Ni_5P_4 surface is most stable at the Ni_3-hollow site, with ΔG_H of −0.43 eV, which is far from the optimum range of $|\Delta G_H| < 0.1$ eV and is in agreement with the first ΔG_H obtained in a prior report.[20] The large first ΔG_H indicates that H_2 is difficult to desorb, and the pristine Ni_5P_4 is not highly active for HER at low hydrogen coverage. After the Ni_3-hollow sites on the pristine Ni_5P_4 surface are fully occupied, the hydrogen will adsorb at the P atop sites with a second ΔG_H of 0.28 eV, which is still far from the optimum range. The HER activity of Ni_5P_4 can be improved if ΔG_H can be reduced on the Ni_3-hollow sites and increased on the P atop sites, where the metal doping strategy would play a critical role.[13]

Based on the results illustrated in Figure 1, the most promising candidates for doping are Zn, Mg, and Ti, which make both the first and second ΔG_H much closer to the optimal range of $|\Delta G_H| < 0.1$ eV than that of pristine Ni_5P_4, suggesting excellent potential for HER. Specifically, Zn doping changes the first ΔG_H from −0.43 eV (pristine Ni_5P_4) to −0.16 eV and the second ΔG_H from 0.28 eV (pristine Ni_5P_4) to −0.01 eV. The first hydrogen occupies the Ni−P bridge site instead of the Ni_3 hollow, whereas the second hydrogen is still located at the P atop site. Similarly, Mg doping changes the first and second ΔG_H to −0.17 and 0.07 eV, respectively. Its first hydrogen also occupies the Ni−P bridge site, but the second hydrogen is located on the Ni−Ni bridge of the Ni−Ni−Mg site. Ti doping brings the first and second ΔG_H to −0.27 and 0.18 eV, respectively. Hydrogen atom binding sites on Ti-doped surfaces are similar to those on the pristine Ni_5P_4 surface. All (Zn, Mg, and Ti) dopants of the surface layer effectively weakened the hollow site's binding energy. Doping with V, Mo, Cu, and Cr lowers either the first or the second ΔG_H closer to the optimal range. However, doping with Fe and Co is ineffective in bringing ΔG_H closer to the optimal range and, therefore, may not be effective in improving the HER performance.

In order to find the key parameters which can easily be used to improve HER activity in rational design, an atomic-scale understanding of the electronic structure of active sites is essential. Figure 2 shows the correlation plot between the M-Ni distance in the M−Ni−Ni hollow on the surface (M is the doped metal) and the lowest 1st and 2nd ΔG_H in eV of the nine transition-metal-doped Ni_5P_4 (001) surfaces. All M−Ni distances are smaller than the Ni−Ni distance in the original Ni_3 hollow site on the pristine Ni_5P_4 (001) surface, except Co.

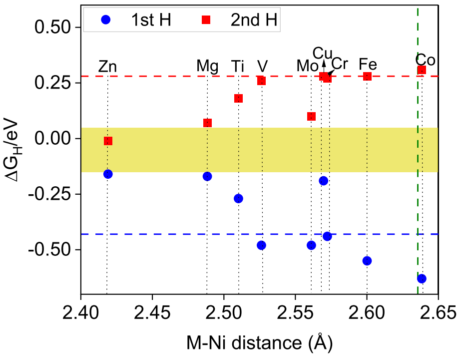

Figure 2. Correlation plot between the M−Ni distance in the M−Ni−Ni hollow on nine transition-metal-doped (M = Zn, Mg, Ti, V, Mo, Cu, Cr, Fe, and Co for data from left to right) Ni_5P_4 (001) surfaces with the Ni_3P_3 termination and the lowest 1st and 2nd ΔG_H calculated by PBE+D3(BJ). The blue and red dotted lines are the lowest ΔG_H values for the first and second hydrogen adsorptions on pristine Ni_5P_4 surfaces, respectively. The green dotted line is the Ni−Ni distance in the Ni_3 hollow on the surface of pristine Ni_5P_4 (001). The deep yellow band highlights the ±0.1 eV region around the optimal ΔG_H = 0 value.

The results indicate that ΔG_H is related to the M−Ni distance even if the hollow site is not the preferred binding site. The smaller M−Ni distance will have a smaller $|\Delta G_H|$ for both first and second hydrogen adsorptions. The Co doping has the longest M-Ni distance, and therefore, its $|\Delta G_H|$ is even larger than the pristine surface. Zn doping largely changes the electronic structure on the surface and yields the smallest M−Ni distance, which makes Zn-doped Ni_5P_4 produce the smallest 1st and 2nd $|\Delta G_H|$, indicating excellent HER performance. This observation suggests that the admixture of Zn induces a chemical pressure-like effect[48] to expand or compress the Ni_3 hollow site, thus improving the HER activity. A direct link between the macroscopic activity via ΔG_H and the atomic-scale property through the geometrical M−Ni bond distance on the intrinsic surface is therefore established. This simple and intuitive M−Ni bond length provides an effective descriptor to drastically reduce the amount of time-consuming calculations and quickly search, design, and optimize the materials with high HER catalytic activity. Here, Zn was chosen as an optimal dopant to improve the HER activity of Ni_5P_4 NCs due to its smaller M-Ni distance, which induces the smallest 1st and 2nd $|\Delta G_H|$.

Synthesis and Characterization of $Ni_{5-x}Zn_xP_4$ NCs. Based on theoretical findings, a series of phase-pure, hexagonal $Ni_{5-x}Zn_xP_4$ NCs with varying compositions were synthesized. The colloidal synthesis of various nickel phosphide ($Ni_{12}P_5$, Ni_2P, Ni_5P_4, and NiP_2) crystal phases can be achieved through the thermal decomposition of a Ni precursor in an OLA stabilizing/reducing solvent along with a TOP phosphorous source/solvent. Previous reports have shown that the crystal phase of nickel phosphides strongly depends on reaction parameters such as the starting P/Ni precursor ratio, reaction temperature, and time.[30,49] In general, phosphorus-rich phases are favored at higher P:Ni ratios, high temperatures, and longer growth times, and subtle changes in synthesis have been shown to yield mixed-phase Ni−P products. Hence, reaction parameters can be manipulated to produce pure compounds. Based on these reports, we were able to establish the appropriate reaction conditions to synthesize Ni_5P_4 NCs without any impurities. We observed that hexagonal Ni_5P_4 particles with no Ni_2P impurities can be reproducibly synthesized under reaction conditions of 340 °C for 4 h using $Ni(acac)_2$ and a nominal P/Ni ratio of 16.7.

$Zn(acac)_2$ was chosen as a Zn source based on its ease of use and its liable acetylacetonate (acac) ligands, similar to $Ni(acac)_2$. The liability of the acac moiety in $Zn(acac)_2$ was reported by Lak et. al.,[50] where acac is reported to disassociate at ∼90 °C under vacuum, leading to a high concentration of monomers necessary for nucleation. Our degassing temperature (120 °C) far exceeded the dissociation temperature, ensuring that sufficient Zn nuclei are available for doping. The introduction of $Zn(acac)_2$ did not affect synthetic conditions, and the bimetallic NCs possessed the hexagonal Ni_5P_4 structure across various Zn compositions with no evidence of segregation. In addition, there was also no evidence of the formation of Zn_3P_2, which is expected to form under higher temperatures (>350 °C) or with more reactive precursors such as diethylzinc ($ZnEt_2$) and tri(trimethylsilyl)phosphine ($P(SiMe_3)_3$).[51,52]

The crystal phase and purity of synthesized $Ni_{5-x}Zn_xP_4$ NCs were confirmed with PXRD. The PXRD patterns of various $Ni_{5-x}Zn_xP_4$ NCs with Zn compositions ranging from $x = 0.0$−1.27 are presented in Figure 3. Each composition possesses a hexagonal crystalline structure characteristic of Ni_5P_4, and all peaks can be indexed to the reference pattern (PDF 04-003-6053). In addition, there is no evidence of any extraneous peaks within any of the patterns that would indicate the presence of any impurities such as Ni_2P, Ni, NiO, or Zn_3P_2. According to Vegard's law, if there is a significant size discrepancy between the dopant and host, a shift in the PXRD pattern is expected. However, there is no observable shift in any of the peaks. This is most evident when comparing the peak at 53.10° across various Zn concentrations (Supporting Information, Figure S1). This observation is not surprising as Zn and Ni are relatively similar in size (Ni 135 pm/Ni^{2+} 0.72 Å−Zn 135 pm/Zn^{2+} 0.74 Å), and therefore a minimal lattice expansion is expected. The crystallite size for each composition was calculated by applying the Scherrer formula to the (214) reflection. The crystallite size for binary Ni_5P_4 is 14.4 nm; however, doping with Zn appeared to have an oscillating effect on crystallite size. This trend is observed as the crystallite size decreases to 14.7 nm when $x = 0.29$, then increases to 15.6 nm when $x = 0.65$, and finally increases to 16.4 nm when $x = 1.27$. This inconsistency in crystallite size can be attributed to the complicated nature of the Ni_5P_4 reference pattern and the inherent peak broadening of NCs.

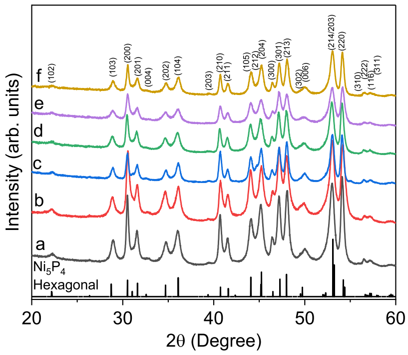

Figure 3. Power X-ray diffraction (PXRD) patterns of binary and zinc-doped Ni_5P_4 NCs with varying zinc concentrations: (a) $x = 0$, (b) $x = 0.10$, (c) $x = 0.29$, (d) $x = 0.65$, (e) $x = 0.84$, and (f) $x = 1.27$. All peaks correspond with the hexagonal Ni_5P_4 reference pattern (JCPDS no. 04-003-6053) shown as vertical black lines.

Initial attempts to determine the elemental compositions of $Ni_{5-x}Zn_xP_4$ NCs were first explored through SEM-EDS. However, this technique was deemed unsuccessful due to the overlap of Ni and Zn L_e X-ray peaks (Ni 0.851 keV and Zn 1.012 keV). ICP-OES was then used for an accurate determination of composition, and it was established that the $Ni_{5-x}Zn_xP_4$ NCs contained zinc concentrations ranging from $x = 0.02$−1.27 or 0.19−16.67 at. % (Table 1). Producing Zn-doped NCs with a substantial Zn concentration was challenging as the nominal Zn composition did not necessarily correlate with the experimental concentration of Zn obtained from ICP-OES, indicating that not all of the nominal Zn concentration is being incorporated into the Ni_5P_4 lattice. In general, an initial doping concentration of 10−20% Zn yielded particles with final Zn compositions ranging from less than 1% to approximately 5%, according to ICP-OES. Whereas NCs with final Zn concentrations of ∼9−17% can be synthesized with a 30−40% starting Zn composition.

One of the major challenges in the synthesis of Ni_5P_4 NCs is generating small monodisperse particles. Previous studies reflect this challenge and demonstrate the issue of small particles aggregating into large/supraparticles.[15,30] However, it

Table 1. Experimental Compositions, Crystallite Sizes, and Average Particle Sizes of Phase Pure Hexagonal $Ni_{5-x}Zn_xP_4$ NCs Produced via Colloidal Synthesis

	elemental composition (ICP-OES)[a]				
sample name	Ni	Zn	P	crystallite size, nm (PXRD)[b]	particle size, nm (TEM)[c]
$Ni_{4.90}Zn_{0.10}P_4$	66.29	1.36	32.36	15.6	14.8 ± 6.6
$Ni_{4.84}Zn_{0.16}P_4$	67.98	2.22	29.80	13.8	18.4 ± 8.1
$Ni_{4.71}Zn_{0.29}P_4$	63.20	3.86	32.94	14.7	26.2 ± 10.9
$Ni_{4.68}Zn_{0.32}P_4$	64.30	4.45	31.25	12.36	25.6 ± 10.8
$Ni_{4.49}Zn_{0.51}P_4$	59.96	6.82	33.22	15.5	20.8 ± 10.2
$Ni_{4.42}Zn_{0.58}P_4$	60.31	7.86	31.82	14.0	28.5 ± 10.1
$Ni_{4.35}Zn_{0.65}P_4$	57.92	9.00	33.08	15.6	24.5 ± 12.5
$Ni_{4.24}Zn_{0.76}P_4$	55.33	9.92	34.75	13.8	22.4 ± 12.0
$Ni_{4.16}Zn_{0.84}P_4$	54.90	11.07	34.03	13.19	18.1± 8.9
$Ni_{3.73}Zn_{1.27}P_4$	48.85	16.67	34.48	16.4	28.7 ± 19.2

[a] Elemental compositions of Ni, Zn, and P were obtained by ICP-OES. Each composition was determined by averaging three individual measurements per sample. [b] Crystallite size was calculated by applying the Scherer equation to the (214) reflection. [c] Average particle size was calculated by measuring 125 individual NCs from TEM images.

has been found that under controlled heating conditions, some of the TOP is retained to act as a stabilizer, and small particles with a narrow dispersity can be formed.[16] $Ni_{5-x}Zn_xP_4$ particle morphology and size dispersity were analyzed using TEM, and their corresponding images are shown in Figure 4. Binary Ni_5P_4 NCs appear to be solid, spherical in morphology, and monodisperse with an average size of 9.2 ± 1.3 nm (Figure 4A). With the introduction of Zn under the same reaction conditions, the particles appear to retain their solid spherical morphology; however, the particles are more polydisperse (Figure 4B−F). The average particle size follows a similar oscillating trend that was observed with crystallite size (Table 1 and Supporting Information, Figures S2 and S3). The average particle size increases to 18.4 ± 8.1 nm when x = 0.16 and further increases to a maximum size of 28.5 ± 10.1 nm when x = 0.58. As the Zn concentration reaches x = 0.84, the average size decreases to 18.1 ± 11.5 nm. Moreover, the population of larger particles appears to increase with increasing Zn, affecting the average particle size more heavily, which can be gleaned from the analysis of the subpopulations present. When x = 0.16, two populations were observed: one subpopulation with an average size of approximately 15 nm, and another subpopulation with an average size of approximately 40 nm. At x = 0.76, three subpopulations are prominent, with average particle sizes of approximately 15, 30, and 42 nm. Since binary NCs are monodisperse, Zn incorporation is most likely affecting the concentration of available nuclei and/or the growth dynamics of the Zn−Ni_5P_4 NCs, resulting in a broader distribution of NCs. HRTEM images of Ni_5P_4 NCs shown in Figure 4K indicate that binary NCs possess a lattice spacing of 0.206 nm corresponding to the (105) plane, while the highest Zn containing $Ni_{3.73}Zn_{1.27}P_4$ NCs have a comparable lattice spacing of 0.205 nm (Figure 4L). The lack of a significant change in lattice spacing indicates that Zn induces no obvious strain on the Ni_5P_4 lattice, which is supported by observations from PXRD patterns where no shifting was observed. Additionally, STEM-EDS maps were used to corroborate the presence of Ni, Zn, and P and to confirm Ni−Zn alloying. The dark field TEM image in Figure 4G shows the presence of 3 particles of various sizes (30.2, 24.1, and 9.0 nm). The resulting STEM-EDS maps validate that Ni, Zn, and P are present and homogeneously distributed throughout the NCs having different sizes (Figure 4H−J). There is no indication of Zn or Zn_3P_2 segregation on the surface or within the particles. As a result, all maps recorded are consistent with the formation of homogeneous $Ni_{5-x}Zn_xP_4$ NCs.

XPS was used to investigate and compare the surface characteristics of Ni_5P_4 and $Ni_{5-x}Zn_xP_4$ NCs. All samples were annealed at 300 °C in 5% H_2:Ar for 4 h to remove residual ligands prior to analysis; therefore, surface charge modulation is absent of any contributions from ligands. Comparing the Ni_5P_4 NCs and $Ni_{4.35}Zn_{0.65}P_4$ NCs, the survey spectra show Ni, O, C, and P peaks present in both materials and an additional Zn peak present in the $Ni_{4.35}Zn_{0.65}P_4$ sample (Supporting Information, Figure S4), which is consistent with STEM studies. The Ni 2p spectrum in both samples exhibits a dominant $Ni^{\delta+}$ species, as indicated by the $2p_{3/2}$ and $2p_{1/2}$ peak positions at 583.17 and 870.42 eV for Ni_5P_4 (Figure 5B) and 583.13 and 870.42 eV for $Ni_{4.35}Zn_{0.65}P_4$ (Figure 5A). Peaks located at 860.39 eV for Ni_5P_4 and 858.79 eV for $Ni_{4.35}Zn_{0.65}P_4$ correspond to $Ni^{\delta+}$ satellites, which have been commonly found in Ni−P samples.[12,16] In addition, the presence of a Ni^{2+} species in the form of NiO is confirmed by a peak at 856.92 eV for Ni_5P_4 and 856.87 eV for $Ni_{4.35}Zn_{0.65}P_4$ NCs.[12,16] In the P 2p region, two doublets are present in both the Ni_5P_4 and the $Ni_{4.35}Zn_{0.65}P_4$ NCs. The doublet at 129.41 and 129.43 eV, for Ni_5P_4 and $Ni_{4.35}Zn_{0.65}P_4$, respectively, corresponds to a metal phosphide surface species.[53] The doublet at 134.48 and 134.82 eV, binary and zinc-doped NCs, respectively, is indicative of the presence of surface $PO_4{}^{3-}$.[12,54] Literature data suggest that the presence of NiO and $PO_4{}^{3-}$ species can be attributed to surface oxidation as the material is exposed to oxygen during the purification process. The presence of NiO and $PO_4{}^{3-}$ surface species is also confirmed in the O spectra (Supporting Information, Figure S5). The major peak within the O1s region was deconvoluted to encompass two peaks: 531.70 and 533.36 eV for Ni_5P_4 NCs and 531.76 and 533.23 eV for $Ni_{4.35}Zn_{0.65}P_4$ NCs. The peak located at 531 eV indicates the phosphate group is the result of P−O surface species, whereas the peak at 533 eV is the result of P═O and/or P−O−P surface species. Both peaks within the O 1s spectra indicate the oxidation of terminal P moieties along the surface. Lastly, the small peak at 528.01 eV suggests metal−oxygen bonding, which also confirms the presence of NiO. The Zn 2p spectrum of $Ni_{4.35}Zn_{0.65}P_4$ suggests a partial positive charge on Zn as indicated by a peak at 1022.43 eV, which is slightly higher in energy than metallic Zn^0 (1021.7 eV).[55] Similar surface characteristics were observed in samples having higher Zn compositions, $Ni_{4.16}Zn_{0.84}P_4$ (Supporting Information, S6 and S7). $Ni_{4.16}Zn_{0.84}P_4$ NCs also display $Ni^{\delta+}$ features, with a $Ni_{3/2}$ peak at 853.05 eV and a $Ni_{1/2}$ peak at 870.48 eV. There is also evidence of Ni^{2+} (NiO) and a $Ni^{\delta+}$ satellite with peaks at 856.92 and 859.58 eV, respectively. A doublet at 129.67 and 134.88 eV in the P 2p region indicates the presence of metal phosphide bonding as well as phosphates. Lastly, the $Zn^{\delta+}$ 1022.42 eV peak in the Zn 2p region remains. Numerous conclusions can be inferred when comparing the effects of Zn doping on the characteristics of surface species. First, the $Ni^{\delta+}$ appears to become less positive as the $Ni_{3/2}$ peak shifts from 853.17 to 853.13 and finally to 853.05 eV as the Zn concentration increases from Ni_5P_4, $Ni_{4.35}Zn_{0.65}P_4$ to $Ni_{4.16}Zn_{0.84}P_4$. While the charge on Ni becomes less positive,

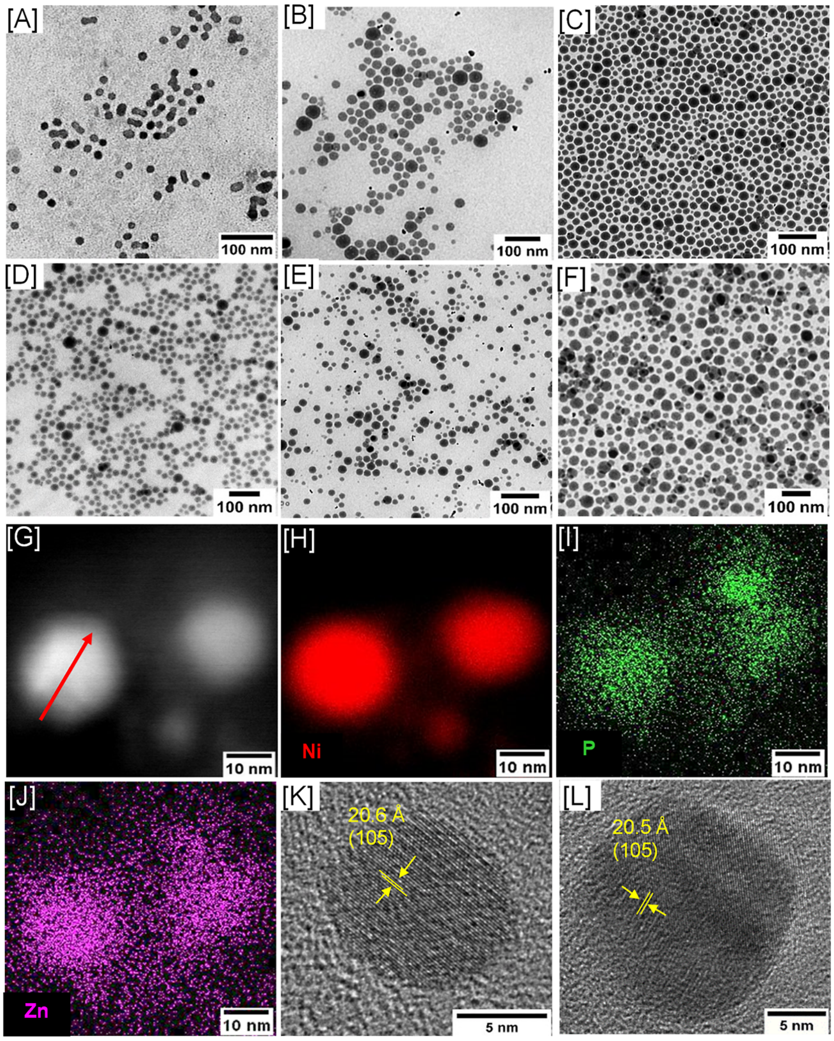

Figure 4. Low resolution TEM images of hexagonal $Ni_{5-x}Zn_xP_4$ NCs with varying compositions: (A) $x = 0$ (9.2 ± 1.3 nm), (B) $x = 0.16$ (18.4 ± 8.1 nm), (C) $x = 0.32$ (25.6 ± 10.8 nm), (D) $x = 0.58$ (28.5 ± 10.1 nm), (E) $x = 0.76$ (22.4 ± 12.0 nm), and (F) $x = 0.84$ (18.1 ± 8.9 nm). (G) Bright field TEM image of $Ni_{3.73}Zn_{1.27}P_4$ NCs along with STEM-EDS maps of (H) Ni, (I) P, and (J) Zn. High resolution TEM images of (K) $x = 0$ and (L) $x = 1.27$ compositions with corresponding lattice spacing measurements for the (105) reflection.

the opposite is observed with P as the partial negative charge increases from 129.41 and 129.43 to 129.67 eV with increasing Zn. As the partial charges on Ni and P vary, there is only a slight alteration in the $Zn^{\delta+}$ peak as it shifts from 1022.43 to 1022.42 eV with increasing Zn. The changes observed in the charges on the Ni and P surface moieties indicate that Zn is modifying the surface polarization of the NCs. These changes reflect the claims made by the theory that zinc alters the binding energy at active sites and may have a significant impact on H binding and, subsequently, HER performance.

Electrocatalytic Activity of $Ni_{5-x}Zn_xP_4$ NCs for HER. The HER activity and stability of $Ni_{5-x}Zn_xP_4$ NCs with varying compositions were investigated via LSV and chronopotentiometry and compared to the benchmark Pt/C (10% wt) catalyst. To fabricate catalyst inks, $Ni_{5-x}Zn_xP_4$ NCs and Pt/C were sonicated with isopropanol and Nafion. Size selection was not attempted, which resulted in ink solutions being an ensemble average of all subpopulations of particles within each sample. Organic surfactant ligands (OLA/TOP) used in the NC synthesis are detrimental for electrocatalysis because they lower the electrochemical active surface area of the catalyst. Therefore, annealing at high temperatures (300−450 °C) in a 5% H_2/Ar atmosphere was employed in the electrode fabrication to ensure ligand removal, increase the ohmic conductivity, and improve the catalyst adhesion to the Ti substrate. For hexagonal Ni_2P NCs, annealing at 450 °C for 2 h was sufficient to remove the surfactant with no changes in crystal structure or morphology.[54] However, experiments performed with $Ni_{5-x}Zn_xP_4$ NCs at 450 °C resulted in a mixture of hexagonal Ni_5P_4 and Ni_2P phases, with a corresponding Rietveld refinement of 56.5% Ni_2P and 43.5% Ni_5P_4 phases (Supporting Information, Figure S8). Thus, all samples were annealed at 300 °C for 4 h to maintain the original crystal structure of Ni_5P_4 and $Ni_{5-x}Zn_xP_4$ NCs. FT-IR spectra of post-annealed $Ni_{5-x}Zn_xP_4$ NCs suggest that annealing at 300 °C for 4 h is sufficient for the removal of residual OLA/TOP ligands, which is evident from the loss of the C−H stretch at 2938 and 2859 cm^{-1}, C═C stretch at 1650 cm^{-1}, C−N stretch at 1468 cm^{-1}, and the C−P stretch at 1068 cm^{-1} (Figure 5F).

The effects of Zn doping of Ni_5P_4 NCs on HER activity and stability were investigated in 1 M KOH and compared with bare Ti foil and Pt/C reference materials in Figure 6A−D and Table 2. Ti foil is known for its high mechanical strength and

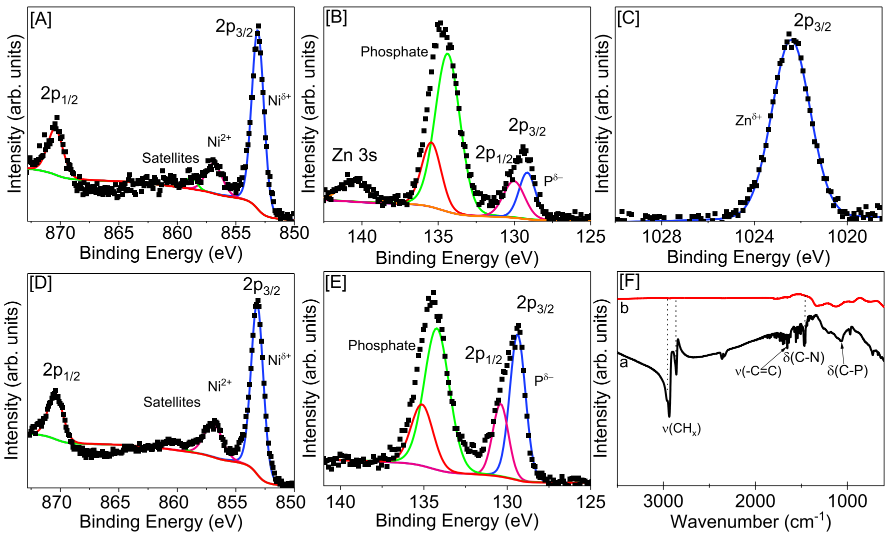

Figure 5. XPS spectra of $Ni_{4.35}Zn_{0.65}P_4$ NCs showing (A) Ni 2p, (B) P 2p, and (C) Zn 2p regions, along with the XPS spectra of Ni_5P_4 NCs showing (D) Ni 2p and (E) P 2p regions. Square symbols represent experimental data, and colored lines are fitted deconvolutions. Samples were annealed for 4 h at 300 °C under a 5% H_2:Ar atmosphere. (F) FTIR spectra of $Ni_{4.16}Zn_{0.84}P_4$ NCs (a) before and after (b) annealing at 300 °C for 4 h.

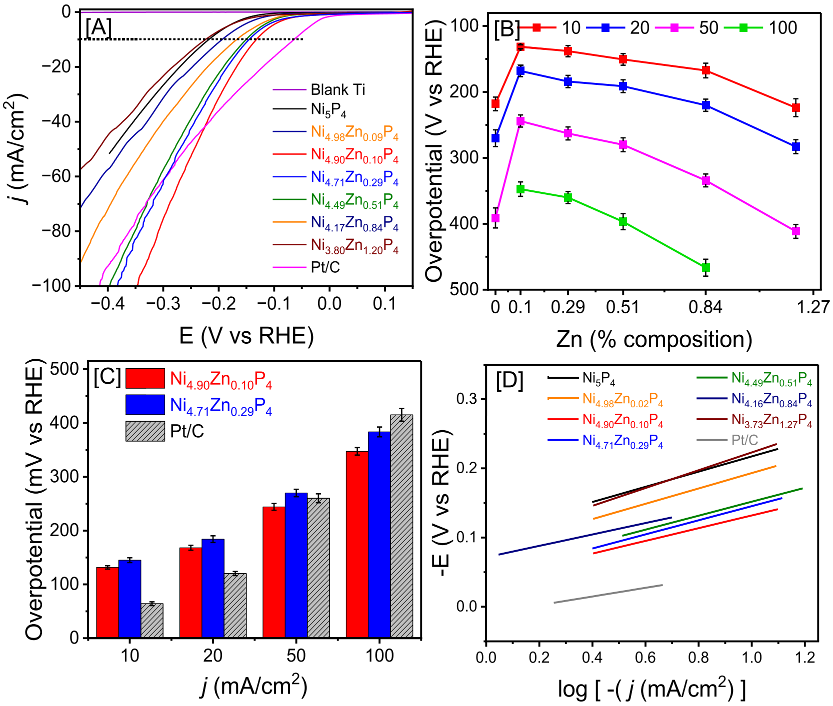

Figure 6. (A) Polarization plots of $Ni_{5-x}Zn_xP_4$ NCs, Ti foil, and commercial Pt/C derived from LSV in 1 M KOH at 5 mV/s scan rate. (B) Variation of overpotentials as a function of Zn concentration of $Ni_{5-x}Zn_xP_4$ NCs. (C) Comparison of overpotentials of $Ni_{4.90}Zn_{0.10}P_4$ and $Ni_{4.71}Zn_{0.29}P_4$ NCs with commercial Pt/C at $j = -10$, -20, -50, and -100 mA/cm^2. (D) Tafel plots of $Ni_{5-x}Zn_xP_4$ NCs and commercial Pt/C derived from LSV in 1 M KOH at 5 mV/s scan rate.

excellent electron conductivity, which by itself showed negligible catalytic activity toward HER, as indicated by the highest onset η_{-1} of 593.1 mV and η_{-10} = 747.1 mV. In contrast, parent Ni_5P_4 NCs produced a lower onset of η_{-1} = 125.8 ± 1.8 mV and η_{-10} = 218.1 ± 6.4 mV, which is consistent with previous reports on Ni_5P_4.[21] However, the admixture of Zn into Ni_5P_4 NCs resulted in significant variations in HER performance with a direct dependence of electrocatalytic activity on Zn concentration, resulting in a volcano-shaped trend shown in Figure 6B. A notable decrease in η is observed as the Zn content increased to $x = 0.1$, whereas an increase in η is observed as the Zn concentration increased from $x = 0.29$ to $x = 1.27$. $Ni_{4.90}Zn_{0.10}P_4$ NCs showed the lowest η of 18.1, 131.6, 168.1, 244.1, and 347.4 mV at $j = -1$, -10, -20, -50, and -100 mA/cm^2, respectively. $Ni_{4.71}Zn_{0.29}P_4$ NCs closely followed with the second lowest overpotential of η_{-10} = 145.10 mV. However, for the highest Zn containing sample ($x = 1.27$), η of 223.8, 283.0, and 411.5 mV were generated at $j = -10$, -20, and -50 mA/cm^2, respectively. These overpotentials exceeded those of the binary Ni_5P_4 NCs,

Table 2. Comparative Elemental Compositions of $Ni_{5-x}Zn_xP_4$ NCs along with Their Corresponding HER Overpotentials at Different Current Densities of −1 (η_{-1}), −10 (η_{-10}), −20 (η_{-20}), −50 (η_{-50}), and −100 (η_{-100}) mA/cm^2 and Tafel Slope Values[a]

	elemental composition[b]			overpotential $(\eta)_{\text{current density (mA/cm}^2)}$[c]				
catalysts	Ni	P	Zn	η_{-10}	η_{-20}	η_{-50}	η_{-100}	Tafel slope
Ni_5P_4	57.52	42.58	0	218.1 ± 10.3	270.1 ± 12.7	391.1 ± 15.2		109.9 ± 2.3
$Ni_{4.98}Zn_{0.02}P_4$	58.50	41.31	0.19	193.8 ± 7.8	247.4 ± 6.1	373.4 ± 7.4		110.8 ± 1.8
$Ni_{4.90}Zn_{0.10}P_4$	66.29	32.36	1.36	131.6 ± 3.1	168.1 ± 4.6	244.1 ± 6.2	347.4 ± 6.9	91.9 ± 3.0
$Ni_{4.71}Zn_{0.29}P_4$	63.20	32.94	3.86	145.1 ± 4.5	184.1 ± 6.3	270.0 ± 6.9	383.6 ± 9.1	101.9 ± 2.1
$Ni_{4.49}Zn_{0.51}P_4$	59.96	33.22	6.82	150.6 ± 8.8	191.2 ± 9.7	280.1 ± 10.5	396.8 ± 11.2	100.8 ± 2.7
$Ni_{4.16}Zn_{0.84}P_4$	54.90	34.03	11.07	167.4 ± 11.1	220.1 ± 9.3	334.2 ± 9.7	466.6 ± 12.8	82.5 ± 2.3
$Ni_{3.73}Zn_{1.27}P_4$	48.85	34.48	16.6	223.8 ± 13.6	283 ± 10.6	411.5 ± 10.5		128.7 ± 3.7
Pt/C				64.1 ± 3.5	120.1 ± 3.8	260.1 ± 8.3	415.3 ± 11.8	70.6 ± 3.5
blank Ti				747.1 ± 2.8				

[a] Electrocatalytic parameters of Ti foil and Pt/C are also included as a reference. [b] Elemental composition of the $Ni_{5-x}Zn_xP_4$ NCs was calculated based on the ICP-OES analysis. [c] Overpotential values were calculated from LSV-derived polarization plots. Values were calculated by averaging three individually prepared samples.

indicating lower catalytic efficiency at the highest Zn concentration. This increase in η can also be attributed to an increased population of larger particles at higher Zn compositions, as evidenced by the TEM images (Figure 4A–F) and the potential increase of catalytically less active Zn sites on the surface. Previous work on $Ni_{2-x}Mo_xP$ NCs also showed lower η values achieved at compositions with up to ~4.2% Mo, indicating there is an optimal dopant concentration that must be achieved for the highest HER activity.[54] At $j = -10$ mA/cm^2, commercial Pt/C exhibited superior HER performance compared to $Ni_{5-x}Zn_xP_4$ NCs, requiring only 64.1 mV of overpotential. However, $Ni_{4.90}Zn_{0.10}P_4$, $Ni_{4.71}Zn_{0.29}P_4$, and $Ni_{4.49}Zn_{0.51}P_4$ outperformed Pt/C at $j = -41.64$, −60.25, and −68.55 mA/cm^2, respectively (Figure 6A). The improved performance at higher current densities can be attributed to the emergence of fresh catalytic sites on the $Ni_{5-x}Zn_xP_4$ NCs, caused by the formation of bubbles when the potential sweeps toward a more negative direction, as depicted in Figure 6A. These findings suggest that $Ni_{5-x}Zn_xP_4$ NCs are excellent candidates for applications that necessitate lower overpotentials at higher current densities.[56,57]

As previously discussed, annealing at 450 °C for 2 h produced a heterogeneous mixture of Ni_5P_4 and Ni_2P phases. Mixed-phase $Ni_2P-Ni_5P_4$ NCs maintained the spherical morphology observed with homogeneous particles; however, mixed-phase systems consisted of smaller particles (8.1 ± 3.0 nm) with a narrower size dispersity (Supporting Information, Figure S9). These heterogeneous particles showed a different HER response compared to phase-pure homogeneous $Ni_{5-x}Zn_xP_4$ NCs and a direct dependence of HER activity on Zn concentration (Supporting Information, Table S1). Among mixed-phase NCs, the heterogeneous particles with $x = 0.51$ possessed the lowest η of 155.1 mV compared to heterogeneous $x = 0.29$ (167.6 mV), $x = 0.33$ (175.1 mV), and $x = 0.84$ (166.9 mV) at $j = -10$ mA/cm^2 (Supporting Information, Figure S10). Similar to the homogeneous $Ni_{5-x}Zn_xP_4$ NCs, the heterogeneous NCs with $x = 0.51$, $x = 0.29$, $x = 0.32$, and $x = 0.84$ compositions outperformed the benchmark Pt/C at higher current densities. However, homogeneous $Ni_{5-x}Zn_xP_4$ NCs displayed a significantly higher HER activity compared to the heterogeneous NCs obtained through annealing at 450 °C. To validate this claim further, a mixed $Ni_5P_4-Ni_2P$ phase NCs, containing 6.07% Zn, was prepared by decreasing the reaction time (Supporting Information, Figure S9). These mixed phase NCs with ~36% Ni_2P showed $\eta_{-10} = 233.1$ mV, which is higher than the overpotential of $x = 0.51$ (6.82% Zn, ~50% Ni_2P) heterogeneous NCs produced via annealing at 450 °C ($\eta_{-10} = 155.1$ mV) (Supporting Information, Figure S11). Overall, heterogeneous NCs produced via annealing and colloidally proved to be less HER active than homogeneous $Ni_{5-x}Zn_xP_4$ NCs. These findings suggest that the HER activity of Zn-doped Ni_5P_4 NCs depends on both the concentration of dopant and phase purity (homogenous vs heterogenous) of $Ni_{5-x}Zn_xP_4$ NCs.

XPS analysis, displayed in Figure 5, reveals that Zn doping affects the surface charge of the NCs, leading to an increase in the negative charge on P and a decrease in the positive charge on Ni. These doping induced effects on surface charge may have a substantial influence on HER kinetics. In an alkaline medium, HER proceeds through either the Volmer–Tafel or Volmer–Heyrovsky reaction mechanisms and involves three primary steps: the one electron reduction of a water molecule and the adsorption of H* on the catalyst surface (Volmer reaction, $H_2O + e^- \rightarrow H^* + OH^-$), followed by the generation of H_2 gas, which can occur through either electrochemical desorption (Heyrovsky reaction, $H_2O + H^* + e^- \rightarrow H_2 + OH^-$) or recombination of two adsorbed H* (Tafel reaction, $2H^* \rightarrow H_2$). To determine the reaction kinetics, Tafel slopes were estimated from the polarization curves of $Ni_{5-x}Zn_xP_4$ and are presented in Figure 6D. Tafel slope values of $Ni_{5-x}Zn_xP_4$ NCs ranged from 82.46 to 128.65 mV/dec, suggesting a Volmer–Heyrovsky type reaction mechanism where the Volmer step is the slower rate-determining step. Binary Ni_5P_4 yielded a Tafel slope of 109.87 mV/dec, while $Ni_{4.16}Zn_{0.84}P_4$ generated the lowest slope of 82.46 ± 0.49 mV/dec. Although $Ni_{4.90}Zn_{0.10}P_4$ displayed the lowest η, these NCs exhibited the second lowest Tafel slope of 92 mV/dec. This suggests an accelerated Volmer step on the catalyst surface upon Zn doping. Other catalysts such as $Ni_{4.98}Zn_{0.02}P_4$, $Ni_{4.71}Zn_{0.29}P_4$, $Ni_{4.49}Zn_{0.51}P_4$, and $Ni_{3.73}Zn_{1.27}P_4$ showed comparable Tafel slopes of 110.84, 101.97, 100.83, and 128.65 mV/dec, respectively, suggesting a similar HER mechanism. Heterogenous Zn-doped samples displayed a comparable range of Tafel slopes (88.9 to 100.1 mV/dec), indicating a similar HER mechanism to homogeneous samples (Supporting Information, Figure S10). This study on $Ni_{5-x}Zn_xP_4$ NCs is consistent with other transition metal phosphide-based

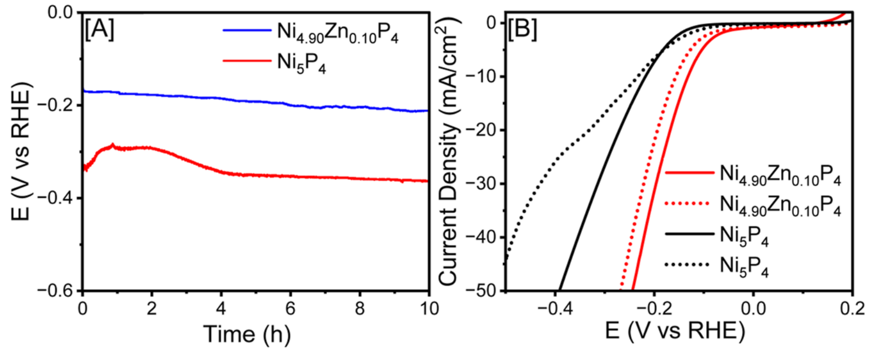

Figure 7. (A) Chronopotentiometry plot of Ni_5P_4 and $Ni_{4.90}Zn_{0.10}P_4$ NCs at -10 mA/cm^2 for 10 h and (B) polarization plots taken before (solid line) and after (dotted line) the chronopotentiometry experiment. Data was collected at room temperature under a N_2 atmosphere.

catalysts, which exhibited a dominant Volmer reaction mechanism. This led us to anticipate that the accelerated Volmer step may be attributed to the enhanced negative charge on P, which would bind more favorably to H. In addition, the less positive Ni moiety would not bind as strongly with polar water molecules or OH^- byproducts compared to binary Ni_5P_4 NCs, which could free up available surface sites for hydrogen adsorption.

Chronopotentiometry was employed to understand the effects of Zn doping on the stability of the material. The stability of binary Ni_5P_4 and $Ni_{4.49}Zn_{0.51}P_4$ NCs was evaluated at a constant $j = -10$ mA/cm^2 in a N_2 saturated 1 M KOH. Figure 7A demonstrates that Ni_5P_4 showed an increase in the HER activity in the initial hour, as the η lowered, which is likely caused of the opening of new catalytic centers. However, after the initial decrease, Ni_5P_4 NCs experienced a rapid increase in η, corresponding to a decrease in HER activity over the following ~8 h. Conversely, $Ni_{4.49}Zn_{0.51}P_4$ demonstrated excellent stability over 10 h, exhibiting only a slight change in η (Figure 7A). To compare the changes in HER activity before and after the chronopotentiometry, a new set of LSV plots was recorded for both Ni_5P_4 and $Ni_{4.49}Zn_{0.51}P_4$ samples and compared with the initial polarization curves of each sample (Figure 7B). Binary Ni_5P_4 showed aminor change in overpotential (η_{-10} = 233.4 mV), which is consistent with chronopotentiometry data. However, as the current density increased, a sharp increase in the η was observed, with a subsequent 23.4 and 33.2% increase in the overpotential to reach $j = -20$ and -50 mA/cm^2, respectively. In contrast, $Ni_{4.49}Zn_{0.51}P_4$ NCs exhibited a 18.6% increase in η at $j = -10$ mA/cm^2 which can be attributed to catalyst removal from the substrate because of extensive H_2 bubble formation.[58] Nevertheless, as the current density increases, the difference between overpotentials before and after chronopotentiometry decreases significantly with only a 15, 10, and 5% change in the overpotentials noted at $j = -20$, -50, and -100 mA/cm^2. This suggests that the admixing of Zn improves both the HER activity and stability of $Ni_{5-x}Zn_xP_4$ NCs.

To evaluate the impact of electrocatalysis on the surface properties of $Ni_{5-x}Zn_xP_4$ NCs, $Ni_{4.16}Zn_{0.84}P_4$ NC electrodes were re-examined with XPS (Supporting Information, Figures S12 and 13). The XPS survey scan shows the presence of Ni, Zn, P, K, and F species. The presence of F can be attributed to the Nafion utilized in the electrode fabrication, whereas K originates from the electrolyte. The HER caused an overall negative shift in all surface species, as observed in the $Ni^{\delta+}$ peak shift to 852.33 eV, $P^{\delta-}$ peak shift to 128.09 eV, and the $Zn^{\delta+}$ peak shifts to 1021.45 eV. In addition to the Ni^{2+} (NiO) peak observed in $Ni_{5-x}Zn_xP_4$ NCs prior to catalysis, a new peak at 855.57 eV is detected, which can be attributed to $Ni(OH)_2$ surface species.[59] The negative peak shift is unsurprising, since electrons are being supplied to the catalysts to facilitate the reduction pathway of the water splitting reaction. Furthermore, it is encouraging that all surface species remained after catalysis, with the exception of a new $Ni(OH)_2$ peak, indicating that the integrity of the material is upheld.

■ CONCLUSIONS

In summary, theoretical and experimental techniques were combined to gain an improved understanding of the influence of heteroatom (Zn) doping on the HER activity and stability of phase-pure Ni_5P_4 NCs without convoluting factors from differences in the morphology and crystal phase. DFT studies indicate that heteroatom doping induces a chemical pressure-like effect, which alters the M−Ni bond length of the M−Ni−Ni hollow site to modulate the surface affinity. Out of nine dopants studied, Zn induced the shortest M−Ni bond length, generating smallest the $|\Delta G_H|$ for first and second hydrogen adsorptions. $Ni_{5-x}Zn_xP_4$ NCs synthesized colloidally retained the solid spherical morphology and hexagonal structure of parent Ni_5P_4 NCs with an increase of average size from 9.2 to 28.5 nm for x = 0.00−1.27 compositions. STEM-EDS elemental maps confirmed the homogeneous ternary alloy formation which has been reinforced through the presence of $Ni^{\delta+}$, $Zn^{\delta+}$, and $P^{\delta-}$ surface moieties in XPS. Surface analysis of $Ni_{5-x}Zn_xP_4$ NCs suggests that Zn incorporation modifies the surface polarization, as the $Ni^{\delta+}$ charge becomes less positive and the $P^{\delta-}$ charge becomes more negative with increasing Zn from x = 0.0−0.84. $Ni_{5-x}Zn_xP_4$ NCs with compositions up to x = 0.84 showed low overpotentials from η_{-10} 131.6 to 193.8 mV, compared to 218.1 mV of the monometallic Ni_5P_4 NCs, with the lowest η achieved at x = 0.10. Although Pt/C proved to be the most efficient catalysis at lower current densities (<−40 mA/cm^2), $Ni_{4.90}Zn_{0.10}P_4$, $Ni_{4.71}Zn_{0.29}P_4$, and $Ni_{4.49}Zn_{0.51}P_4$ NCs outperformed the Pt/C at higher current densities (>−40 mA/cm^2). A Volmer−Heyrovsky HER mechanism was determined for all NCs, and an enhanced Volmer step was observed with $Ni_{5-x}Zn_xP_4$ NCs, where Tafel slopes decreased from 109.87 mV/dec for Ni_5P_4 NCs to 82.46 and 92.0 mV/dec for $Ni_{4.16}Zn_{0.84}P_4$ and $Ni_{4.90}Zn_{0.10}P_4$ NCs, respectively. The enhanced Volmer step can be attributed to the modified surface polarization initiated by the larger $P^{\delta-}$ charge and the weaken Ni_3 binding sites observed in Zn-doped samples, which would favor more H adsorption in a protondeficient alkaline solution. Zn incorporation also improves the material's stability particularly at higher current densities as the η of $Ni_{4.49}Zn_{0.51}P_4$ NCs only increased by 15, 10, and 5%, at $j = -20$, -50 and -100 mA/cm^2, respectively, while Ni_5P_4 NCs noted 23.4 and 33.2% increase at $j = -20$ and -50 mA/cm^2. Through an atomic-scale understanding of heteroatom doping, earth-abundant $Ni_{5-x}Zn_xP_4$ NCs become an additional tool in the quest for highly efficient HER electrocatalysts.

■ ASSOCIATED CONTENT

Supporting Information

The Supporting Information is available free of charge at https://pubs.acs.org/doi/10.1021/acs.chemmater.3c01229.

> PXRD patterns of $Ni_{5-x}Zn_xP_4$ NCs with various Zn compositions; particle size histograms of $Ni_{5-x}Zn_xP_4$ NCs; XPS survey scans of Ni_5P_4 and $Ni_{4.35}Zn_{0.65}P_4$ NCs; O (1s) XPS spectra of Ni_5P_4 and $Ni_{4.35}Zn_{0.65}P_4$ NCs; XPS survey scan of $Ni_{4.16}Zn_{0.84}P_4$ NCs; XPS spectra of $Ni_{4.16}Zn_{0.84}P_4$ NCs; PXRD patterns of pre and post annealed Ni_5P_4 NCs; low resolution TEM images and particle size histograms of heterogenous Zn−Ni_2P−Ni_5P_4 generated synthetically and through annealing; compilation table comparing the effect of elemental composition on overpotential and Tafel slopes for electrocatalytic HER in N_2 saturated 1 M KOH; polarization plots and Tafel plots of heterogeneous Zn-doped Ni_2P−Ni_5P_4 NCs; polarization plot of heterogeneous 6.07% Zn-doped Ni_2P−Ni_5P_4 NCs; XPS survey scan and Ni (2p), P (2p), Zn (2p), and O (1s) XPs spectra of $Ni_{4.12}Zn_{0.88}P_4$ NCs after HER; and compilation table of electrocatalytic data of literature reports for heteroatom-doped Ni_5P_4 (PDF)

■ AUTHOR INFORMATION

Corresponding Author

Indika U. Arachchige − *Department of Chemistry, Virginia Commonwealth University, Richmond, Virginia 23284-2006, United States;* orcid.org/0000-0001-6025-5011; Email: iuarachchige@vcu.edu

Authors

Lisa S. Graves − *Department of Chemistry, Virginia Commonwealth University, Richmond, Virginia 23284-2006, United States*

Rajib Sarkar − *Department of Chemistry, Virginia Commonwealth University, Richmond, Virginia 23284-2006, United States*

Ka Un Lao − *Department of Chemistry, Virginia Commonwealth University, Richmond, Virginia 23284-2006, United States;* orcid.org/0000-0002-3993-536X

Complete contact information is available at: https://pubs.acs.org/10.1021/acs.chemmater.3c01229

Author Contributions

L.S.G. and R.S. contributed equally for this work. L.S.G. completed the synthesis and physical characterization studies and R.S. completed all electrocatalytic studies. The manuscript was written through the contributions of all authors. All authors have given approval to the final version of the manuscript.

Notes

The authors declare no competing financial interest.

■ ACKNOWLEDGMENTS

The authors gratefully acknowledge the financial support by the US National Science Foundation CHE-2154747 award, VCU Presidential Research Quest Fund, and the Department of Chemistry, Virginia Commonwealth University. R.S. acknowledges the support from the Dissertation Research Fellowship. We thank Griffin Spence and Drew Spera for their help with HRTEM and STEM analysis.

■ REFERENCES

(1) Turner, J.; Sverdrup, G.; Mann, M. K.; Maness, P.-C.; Kroposki, B.; Ghirardi, M.; Evans, R. J.; Blake, D. Renewable Hydrogen Production. *Int. J. Energy Res.* **2008**, *32*, 379−407.

(2) Li, Y.; Sun, Y.; Qin, Y.; Zhang, W.; Wang, L.; Luo, M.; Yang, H.; Guo, S. Recent Advances on Water-Splitting Electrocatalysis Mediated by Noble-Metal-Based Nanostructured Materials. *Adv. Energy Mater.* **2020**, *10*, 1903120.

(3) Lasia, A. Hydrogen Evolution Reaction. *Handbook of Fuel Cells-Fundamentals, Technology and Applications*; Wiley, 2003; pp 416−440.

(4) Sarkar, R.; Farghaly, A.; Arachchige, I. U. Oxidative Self-Assembly of Au/Ag/Pt Alloy Nanoparticles into High Surface Area, Mesoporous, and Conductive Aerogels for Methanol Electro-Oxidation. *Chem. Mater.* **2022**, *34*, 5874−5887.

(5) Xiaohui, J.; Tingting, B.; Lijun, Z.; Yulu, Z.; Yuzhi, X.; Daohong, X. Progress in the Preparation and Application of Supported Nickel Phosphide Catalysts. *Petrochem. Technol.* **2015**, *44*, 1409−1416.

(6) Oyama, S. T.; Gott, T.; Zhao, H.; Lee, Y. K. Transition Metal Phosphide Hydroprocessing Catalysts: A Review. *Catal. Today* **2009**, *143*, 94−107.

(7) Bowker, R. H.; Ilic, B.; Carrillo, B. A.; Reynolds, M. A.; Murray, B. D.; Bussell, M. E. Carbazole Hydrodenitrogenation over Nickel Phosphide and Ni-Rich Bimetallic Phosphide Catalysts. *Appl. Catal. A Gen.* **2014**, *482*, 221−230.

(8) Wei, Q.; Liu, X.; Zhou, Y.; Xu, Z.; Zhang, P.; Liu, D. A Promising Catalyst for Hydrodesulfurization: Ni_2P-A DFT Study. *Catal. Today* **2020**, *353*, 39−46.

(9) Golubeva, M. A.; Zakharyan, E. M.; Maximov, A. L. Transition Metal Phosphides (Ni, Co, Mo, W) for Hydrodeoxygenation of Biorefinery Products (a Review). *Pet. Chem.* **2020**, *60*, 1109−1128.

(10) Ray, A.; Sultana, S.; Paramanik, L.; Parida, K. M. Recent Advances in Phase, Size and Morphology-Oriented Nanostructured Nickel Phosphide for Overall Water Splitting. *J. Mater. Chem. A* **2020**, *8*, 19196−19245.

(11) Khalafallah, D.; Sarkar, R.; Demir, M.; Abdelrazek Khalil, K.; Hong, Z.; Farghaly, A. A. Heteroatoms-Doped Carbon Nanotubes for Energy Applications. *Handbook of Carbon Nanotubes*; Springer, 2022; pp 525−556.

(12) Pan, Y.; Liu, Y.; Zhao, J.; Yang, K.; Liang, J.; Liu, D.; Hu, W.; Liu, D.; Liu, Y.; Liu, C. Monodispersed Nickel Phosphide Nanocrystals with Different Phases: Synthesis, Characterization and Electrocatalytic Properties for Hydrogen Evolution. *J. Mater. Chem. A* **2015**, *3*, 1656−1665.

(13) Wang, Y.; Kong, B.; Zhao, D.; Wang, H.; Selomulya, C. Strategies for Developing Transition Metal Phosphides as Heterogeneous Electrocatalysts for Water Splitting. *Nano Today* **2017**, *15*, 26−55.

(14) Laursen, A. B.; Wexler, R. B.; Whitaker, M. J.; Izett, E. J.; Calvinho, K. U. .; Hwang, S.; Rucker, R.; Wang, H.; Li, J.; Garfunkel, E.; et al. Climbing the Volcano of Electrocatalytic Activity While Avoiding Catalyst Corrosion: Ni_3P, a Hydrogen Evolution Electrocatalyst Stable in Both Acid and Alkali. *ACS Catal.* **2018**, *8*, 4408−4419.

(15) Laursen, A. B.; Patraju, K. R.; Whitaker, M. J.; Retuerto, M.; Sarkar, T.; Yao, N.; Ramanujachary, K. V.; Greenblatt, M.; Dismukes, G. C. Nanocrystalline Ni_5P_4: A Hydrogen Evolution Electrocatalyst of Exceptional Efficiency in Both Alkaline and Acidic Media. *Energy Environ. Sci.* **2015**, *8*, 1027−1034.

(16) Li, H.; Lu, S.; Sun, J.; Pei, J.; Liu, D.; Xue, Y.; Mao, J.; Zhu, W.; Zhuang, Z. Phase-Controlled Synthesis of Nickel Phosphide Nanocrystals and Their Electrocatalytic Performance for the Hydrogen Evolution Reaction. *Chem. Eur. J.* **2018**, *24*, 11748−11754.

(17) Wexler, R. B.; Martirez, J. M. P.; Rappe, A. M. Active Role of Phosphorus in the Hydrogen Evolving Activity of Nickel Phosphide (0001) Surfaces. *ACS Catal.* **2017**, *7*, 7718−7725.

(18) Elmutasim, O.; Sajjad, M.; Singh, N.; AlWahedi, Y.; Polychronopoulou, K. Combined DFT and Mircokinetic Modeling Study of SO_2 Hydrodesulfurization Reaction on Ni_5P_4 Catalyst. *Appl. Surf. Sci.* **2021**, *559*, 149872.

(19) Zhang, T.; Yang, K.; Wang, C.; Li, S.; Zhang, Q.; Chang, X.; Li, J.; Li, S.; Jia, S.; Wang, J.; et al. Nanometric Ni_5P_4 Clusters Nested on $NiCo_2O_4$ for Efficient Hydrogen Production via Alkaline Water Electrolysis. *Adv. Energy Mater.* **2018**, *8*, 1801690.

(20) Hu, J.; Cao, X.; Zhao, X.; Chen, W.; Lu, G.; Dan, Y.; Chen, Z. Catalytically Active Sites on Ni_5P_4 for Efficient Hydrogen Evolution Reaction from Atomic Scale Calculation. *Front. Chem.* **2019**, *7*, 444.

(21) He, Q.; Tian, D.; Jiang, H.; Cao, D.; Wei, S.; Liu, D.; Song, P.; Lin, Y.; Song, L. Achieving Efficient Alkaline Hydrogen Evolution Reaction Over a Ni_5P_4 Catalyst Incorportating Single-Atomic Ru Sites. *Adv. Mater.* **2020**, *32*, 1906972.

(22) Wexler, R. B.; Martirez, J. M. P.; Rappe, A. M. Stable Phosphorus-Enriched (0001) Surfaces of Nickel Phosphides. *Chem. Mater.* **2016**, *28*, 5365−5372.

(23) Rao, Y.; Wang, S.; Zhang, R.; Jiang, S.; Chen, S.; Yu, Y.; Bao, S.; Xu, M.; Yue, Q.; Xin, H.; et al. Nanoporous V-Doped Ni_5P_4 Microsphere: A Highly Efficient Electrocatalyst for Hydrogen Evolution Reaction at All pH. *ACS Appl. Mater. Interfaces* **2020**, *12*, 37092−37099.

(24) Hernandez, A. B.; Ariga, H.; Takakusagi, S.; Kinoshita, K.; Suzuki, S.; Otani, S.; Oyama, S. T.; Asakura, K. Dynamical LEED Analysis of Ni_2P (0001)-1x1: Evidence for P-Covered Surface Structure. *Chem. Phys. Lett.* **2011**, *513*, 48−52.

(25) Owens-Baird, B.; Kolen'ko, Y. V.; Kovnir, K. Structure-Activity Relationships for Pt-Free Metal Phosphide Hydrogen Evolution Electrocatalysts. *Chem. Eur. J.* **2018**, *24*, 7298−7311.

(26) Ma, T.; Qiu, Y.; Zhang, Y.; Ji, X.; Hu, P.-A. Iron-Doped Ni_5P_4 Ultrathin Nanoporous Nanosheets for Water Splitting and On-Demand Hydrogen Release via $NaBH_4$ Hydrolysis. *ACS Appl. Nano Mater.* **2019**, *2*, 3091−3099.

(27) Miao, C.; Zang, Y.; Wang, H.; Zhuang, X.; Han, N.; Yin, Y.; Ma, Y.; Chen, M.; Dai, Y.; Yip, S.; et al. Tunable D-Band Centers of Ni_5P_4 Ultra-Thin Nanosheets for Highly-Efficient Hydrogen Evolution Reaction. *Adv. Mater. Interfaces* **2022**, *9*, 2200739.

(28) Xiao, X.; Wu, X.; Wang, Y.; Zhu, K.; Liu, B.; Cai, X.; Yang, T.; Xu, X.; Zhang, D. Co-Doped Porous Ni_5P_4 Nanoflower: An Efficient Hydrogen Evolution Electrocatalyst with High Activity and Electrochemical Stability. *Catal. Commun.* **2020**, *138*, 105957.

(29) An, C.; Wang, Y.; Jiao, P.; Wu, S.; Gao, L.; Zhu, C.; Li, J.; Hu, N. Se-Doped Ni_5P_4 Nanocatalysts for High-Efficiency Hydrogen Evolution Reaction. *Catalysts* **2022**, *12*, 1055.

(30) Li, D.; Senevirathne, K.; Aquilina, L.; Brock, S. L. Effect of Synthetic Levers on Nickel Phosphide Nanoparticle Formation: Ni_5P_4 and NiP_2. *Inorg. Chem.* **2015**, *54*, 7968−7975.

(31) Liyanage, D.; Spera, D. Z.; Sarkar, R.; Troesch, B. P.; Nakagawara, T. A.; Ozgur, U.; Arachchige, I. U. CdSe/Ag Hybrid Aerogels: Integration of Plasmonic and Excitonic Properties of Metal-Semiconductor Nanostructures via Sol-Gel Assembly. *Adv. Photonics Res.* **2022**, *3*, 2200026.

(32) Kresse, G.; Furthmuller, J. Efficient Iterative Schemes for *Ab Initio* Total-Energy Calculations Using a Plane-Wave Basis Set. *Phys. Rev. B* **1996**, *54*, 11169−11186.

(33) Hu, J.; Zheng, S.; Zhao, X.; Yao, X.; Chen, Z. A Theoretical Study on the Surface and Interfacial Properties of Ni_3P for the Hydrogen Evolution Reaction. *J. Mater. Chem. A* **2018**, *6*, 7827−7834.

(34) Huang, A.; Dinh, K. N.; Sun, X.; Yan, Q.; Wang, Z. Surface Treated Nickel Phosphide Nanosheet with Oxygen as Highly Efficient Bifunctional Electrocatalysts for Overall Water Splitting. *Appl. Surf. Sci.* **2019**, *496*, 143741.

(35) Nørskov, J. K.; Bligaard, T.; Logadottir, A.; Kitchin, J. R.; Chen, J. G.; Pandelov, S.; Stimming, U. Trends in the Exchange Current for Hydrogen Evolution. *J. Electrochem. Soc.* **2005**, *152*, J23−J26.

(36) Hansen, M. H.; Stern, L.-A.; Feng, L.; Rossmeisl, J.; Hu, X. Widely Available Active Sites on Ni_2P for Electrochemical Hydrogen Evolution-Insights from First Principles Calculation. *Phys. Chem. Chem. Phys.* **2015**, *17*, 10823−10829.

(37) Tang, Q.; Jiang, D. e. Mechanism of Hydrogen Evolution Reaction on 1T-MoS_2 from First Principles. *ACS Catal.* **2016**, *6*, 4953−4961.

(38) Sun, H.; Min, Y.; Yang, W.; Lian, Y.; Lin, L.; Feng, K.; Deng, Z.; Chen, M.; Zhong, J.; Xu, L.; et al. Morphological and Electronic Tuning of Ni_2P Through Iron Doping Toward Highly Efficient Water Splitting. *ACS Catal.* **2019**, *9*, 8882−8892.

(39) Liu, P.; Rodriguez, J. A. Catalysts for Hydrogen Evolution from the [NiFe] Hydrogenase to the Ni_2P (001) Surface. *J. Am. Chem. Soc.* **2005**, *127*, 14871−14878.

(40) Greeley, J.; Jaramillo, T. F.; Bonde, J.; Chorkendorff, I.; Nørskov, J. K. Computational High-Throughput Screening of Electrocatalytic Materials for Hydrogen Evolution. *Nat. Mater.* **2006**, *5*, 909−913.

(41) Zheng, Y.; Jiao, Y.; Zhu, Y.; Li, L. H.; Han, Y.; Chen, Y.; Du, A.; Jaroniec, M.; Qiao, S. Z. Hydrogen Evolution by a Metal-Free Electrocatalyst. *Nat. Commun.* **2014**, *5*, 3783.

(42) Hakala, M.; Laasonen, K. Hydrogen Adsorption Trends on Al-Doped Ni_2P Surfaces for Optimal Catalyst Design. *Phys. Chem. Chem. Phys.* **2018**, *20*, 13785−13791.

(43) Partanen, L.; Hakala, M.; Laasonen, K. Hydrogen Adsorption Trends on Various Metal-Doped Ni_2P Surfaces for Optimal Catalysts Design. *Phys. Chem. Chem. Phys.* **2019**, *21*, 184−191.

(44) Partanen, L.; Alberti, S.; Laasonen, K. Hydrogen Adsorption Trends on Two Metal-Doped Ni_2P Surfaces for Optimal Catalyst Design. *Phys. Chem. Chem. Phys.* **2021**, *23*, 11538−11547.

(45) Perdew, J. P.; Burke, K.; Ernzerhof, M. Generalized Gradient Approximation Made Simple. *Phys. Rev. Lett.* **1996**, *77*, 3865−3868.

(46) Girmme, S.; Antony, J.; Ehrlich, S.; Krieg, H. A Consistent and Accurate Ab Initio Parametrization of Density Functional Dispersion Correction (DFT-D) for the 94 Elements H-Pu. *J. Chem. Phys.* **2010**, *132*, 154104.

(47) Grimme, S.; Ehrlich, S.; Goerigk, L. Effect of the Damping Function in Dispersion Corrected Density Functional Theory. *J. Comput. Chem.* **2011**, *32*, 1456−1465.

(48) Wexler, R. B.; Martirez, J. M. P.; Rappe, A. M. Chemical Pressure-Driven Enhancement of the Hydrogen Evolving Activity of Ni_2P from Nonmetal Surface Doping Interpreted via Machine Learning. *J. Am. Chem. Soc.* **2018**, *140*, 4678−4683.

(49) Wang, J.; Johnston-Peck, A. C.; Tracy, J. B. Nickel Phosphide Nanoparticles with Hollow, Solid, and Amorphous Structures. *Chem. Mater.* **2009**, *21*, 4462−4467.

(50) Lak, A.; Kahmann, T.; Schaper, S. J.; Obel, J.; Ludwig, F.; Müller-Buschbaum, P.; Lipfert, J. The Dissociation Rate of Acetylacetonate Ligands Governs the Size of Ferrimagnetic Zinc Ferrite Nanocubes. *Appl. Mater. Interfaces* **2020**, *12*, 217−226.

(51) Hosnay Mobarok, M.; Luber, E. J.; Bernar, G. M.; Peng, L.; Wasylishen, R. E.; Buriak, J. M. Phase-Pure Crystalline Zinc Phosphide Nanoparticles: Synthetic Approaches and Characterization. *Chem. Mater.* **2014**, *26*, 1952−1935.

(52) Ho, M. Q.; Esteves, R. J. A.; Kedarnath, G.; Arachchige, I. U. Size-Dependent Optical Properties of Luminescent Zn_3P_2 Quantum Dots. *J. Phys. Chem. C* **2015**, *119*, 10576−10584.

(53) Carenco, S.; Liu, Z.; Salmeron, M. The Birth of Nickel Phosphide Catalysts: Monitoring Phosphorus Insertion into Nickel. *Chem. Catal. Chem.* **2017**, *9*, 2318−2323.

(54) Eladgham, E. H.; Rodene, D. D.; Sarkar, R.; Arachchige, I. U.; Gupta, R. B. Electrocatalytic Activity of Bimetallic Ni-Mo-P Nanocrystals for Hydrogen Evolution Reaction. *Appl. Nano Mater.* **2020**, *3*, 8199−8207.

(55) Ji, S.; Li, J.; Li, J.; Song, C.; Wang, S.; Wang, K.; Hui, K. S.; Zha, C.; Zheng, Y.; Dinh, D. A.; et al. Dynamic Reversible Evolution of Solid Electrolyte Interface in Nonflammable Triethyl Phosphate Electrolyte Enabling Safe and Stable Potassium-Ion Batteries. *Adv. Funct. Mater.* **2022**, *32*, 2200771.

(56) Zhu, J.; Hu, L.; Zhao, P.; Lee, L. Y. S.; Wong, K. Y. Recent Advances in Electrocatalytic Hydrogen Evolution Using Nanoparticles. *Chem. Rev.* **2020**, *120*, 851−918.

(57) Zhu, Y.; Chen, H. C.; Hsu, C. S.; Lin, T. S.; Chang, C. J.; Chang, S. C.; Tsai, L. D.; Chen, H. M. Operando Unraveling of the Structural and Chemical Stability of P-Substituted $CoSe_2$ Electrocatalysts toward Hydrogen and Oxygen Evolution Reactions in Alkaline Electrolyte. *ACS Energy Lett.* **2019**, *4*, 987−994.

(58) McKone, J. R.; Sadtler, B. F.; Werlang, C. A.; Lewis, N. S.; Gray, H. B. Ni-Mo Nanopowders for Efficient Electrochemical Hydrogen Evolution. *ACS Catal.* **2013**, *3*, 166−169.

(59) Liyanage, D. R.; Danforth, S. J.; Liu, Y.; Bussell, M. E.; Brock, S. L. Simultaneous Control of Composition, Size, and Morphology in Discrete $Ni_{2-x}Co_xP$ Nanoparticles. *Chem. Mater.* **2015**, *27*, 4349−4357.